Eur. Phys. J. D (2024)78:108
https://doi.org/10.1140/epjd/s10053-024-00899-3

THE EUROPEAN PHYSICAL JOURNAL D

Regular Article - Atomic and Molecular Collisions

The influence of experimental conditions on absolute beam density measurements for NH_3 and H

Rahul Pandey[1,a], Lok Yiu Wu[1,2], Lucy Morris[1], Paul Regan[1], and Brianna R. Heazlewood[1,b]

[1] Department of Physics, University of Liverpool, Liverpool L69 7ZE, UK
[2] Physical and Theoretical Chemistry Laboratory, University of Oxford, South Parks Road, Oxford OX1 3QZ, UK

Received 23 May 2024 / Accepted 23 July 2024

Abstract. In order to establish important reaction properties, such as rate coefficients, it is often necessary to know the number of reactants that are present in an interaction region. The absolute number densities of pulsed supersonic molecular (NH_3) and atomic (H) beams are reported using a laser-based detection method, under a range of experimental conditions including photolysis, Zeeman deceleration, and magnetic focusing. Time-averaged densities of $(3.6 \pm 2.7) \times 10^4\,\mathrm{cm}^{-3}$ are reported for successfully Zeeman-decelerated and magnetically focused H atoms, generated by the photodissociation of precursor NH_3 molecules. Without the magnetic guide components in the beamline, the density of the target radicals of interest is somewhat lower, at $(2.5 \pm 1.8) \times 10^4\,\mathrm{cm}^{-3}$. The average density of the undecelerated H atom beam is approximately an order of magnitude higher $(2.9 \pm 1.9) \times 10^5\,\mathrm{cm}^{-3}$, with the average density of the molecular ammonia beam over two orders of magnitude higher again $(5.1 \pm 2.9) \times 10^7\,\mathrm{cm}^{-3}$. The average number densities measured for the two different species of interest in this work span more than three orders of magnitude. These findings highlight the need for accurate and precise experimental measurements of number densities—for each species of interest, under the appropriate experimental conditions—before doing absolute rate coefficient calculations.

1 Introduction

The ability to study gas-phase reactions precisely, where the properties of the reactants are known and the reaction conditions carefully controlled, is essential for understanding the chemistry occurring in a wide range of gas-phase environments. Supersonic molecular beams have long been a staple in a researcher's toolkit for studying gas-phase chemical reactivity. Expanding a gas from a high-pressure reservoir, through a small aperture, and into a vacuum chamber produces a high-intensity beam with a narrow velocity distribution and low internal temperature. The resulting beam can subsequently be intersected by a second beam of reactants (as seen in a crossed beam set-up), or directed towards a stationary target (such as an ion trap), amongst other applications. When using supersonic beams to study bimolecular reaction systems, it is important to ascertain the absolute number densities of the beams—without the absolute number density, only relative rate coefficients can be obtained.

A number of methods have been developed for estimating the density of an atomic or molecular beam, such as those based on the principles governing supersonic expansions [1]. Several manufacturers of pulsed valves have also reported the densities of atomic and molecular beams that can be obtained under different sets of experimental conditions [2–4]. These approaches can provide useful estimates for the expected beam density under certain circumstances. In situations where additional elements are introduced—for example, when components of a beam are manipulated using Stark or Zeeman decelerators, or by a hexapole—it is challenging to rely on predicted molecular beam densities. In such instances, it is typically necessary to experimentally measure the density of the species of interest in the beam.

It has been previously demonstrated that beam densities can be obtained from laser-induced fluorescence (LIF) signal, using the relation $n = \frac{N_{\mathrm{total}}}{0.5V\Omega D_{\mathrm{eff}}}$, where n is the absolute beam density, N_{total} is the number of photons per laser shot observed by LIF, V is the volume probed by the laser, Ω is the solid angle observed by the photomultiplier tube, D_{eff} is the detection efficiency, and 0.5 is a scaling factor included to account for the saturated condition of LIF [5]. One of the main challenges associated with this LIF-based method is determining an accurate solid angle for the collection of flu-

Rahul Pandey and Lok Yiu Wu have contributed equally to this work

[a] e-mail: rahul.pandey@liverpool.ac.uk (corresponding author)
[b] e-mail: b.r.heazlewood@liverpool.ac.uk (corresponding author)

Published online: 20 August 2024

orescence signal [6]. Furthermore, the method is dependent on the species of interest exhibiting a suitable LIF scheme. Another technique has seen the density of a filtered molecular beam measured using a quadrupole mass spectrometer [7]. While using a quadrupole mass spectrometer (such as a residual gas analyser, RGA) to obtain beam densities does not rely on the species of interest possessing a LIF scheme, there are also instances where this approach is not appropriate. For example, it may not be possible to position the RGA at the point where reactions occur, the response time of the RGA can inhibit the recording of peak densities for pulsed molecular beams, and it can be difficult to account for background signal in seeded beams where the species of interest and the carrier gas have similar masses.

In this article, we apply an alternative laser-based method first demonstrated in [8] to obtain absolute number densities for atomic and molecular beams that traverse a Zeeman decelerator and magnetic guide set-up for the first time. Interestingly, the presence of magnetic guide components in the beamline does not decrease the density of the target radicals of interest. Indeed, the presence of two Halbach arrays serves to increase the absolute density of target radical species. Our findings are discussed in the context of previous laser-based studies where the collection of fluorescence is not required [8–11]. The number densities we obtain are also compared to previous measurements of molecular beam densities, recorded under different sets of conditions. The wide range of densities observed in this and previous work, spanning many orders of magnitude, evidences the impact that different variable parameters can have on the absolute number densities obtained. Finally, given this large degree of variability, the results highlight the need for accurate experimental measurements (in place of estimates) where beams are used in reaction studies.

2 Methods

2.1 Experimental set-up

The experimental apparatus adopted for the beam density measurements is shown in Fig. 1. As the set-up has been previously described in detail [12–14], only the key parameters are provided here. Measurements are taken for both ammonia (molecular) and hydrogen (atomic) beams, under different sets of experimental conditions. For experiments involving H atoms, a mixture of 10% NH_3 seeded in Kr is supersonically expanded into a high-vacuum chamber with a stagnation pressure of 5 bar. NH_3 molecules are photodissociated by an ArF excimer (GAM EX5, 0.35 mJ/pulse) at 193 nm in a quartz capillary attached to the face plate of the pulsed valve, forming H atoms. The H atoms traverse a skimmer and then pass through a 12-stage Zeeman decelerator. As hydrogen atoms possess an unpaired electron (i.e. they are radicals), they can

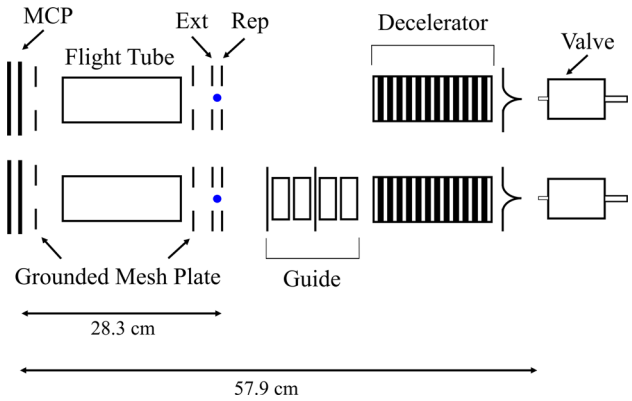

Fig. 1 Schematic diagram of the experimental set-up, without (top) and with (bottom) the magnetic guide components positioned along the beamline. The elements include (from right to left) the pulsed valve, skimmer, Zeeman decelerator, magnetic guide (present only in the bottom schematic), and the time-of-flight stack with repeller (Rep), extractor (Ext), flight tube, and MCP detector. Species are ionised at the point shown in blue between the Rep and Ext plates

be manipulated by external magnetic fields. When the Zeeman decelerator is in operation, a proportion of H atoms in low-field-seeking quantum states are decelerated to selected final velocities through the application of precisely timed current sequences to the Zeeman decelerator coils (inducing magnetic fields within the coils) [12,15]. After the Zeeman decelerator, the beam enters a region where a magnetic guide [13] can be lowered into the beam path. The magnetic guide consists of four Halbach arrays and two skimming blades, the vertical positions of which can all be adjusted *in vacuo*. The displacements of each Halbach array pair or blade with respect to the beam axis can deflect and focus target H atoms, as described in [16]. Downstream of the magnetic guide, the H atoms reach the interaction region where they are detected by a focused dye laser (with energy of up to 1.4 mJ/pulse) using a (2+1) resonance-enhanced multiphoton ionisation (REMPI) scheme at 243.13 nm, intersecting the atomic beam orthogonally.

For ammonia beam density measurements, a gas mixture of 5% NH_3 seeded in Kr is used. The molecular beam expands through the same pulsed valve, but without the excimer laser intersecting the beam. The decelerator coils have no fields applied to them, but they are still physically present in the vacuum chamber; the magnetic guide components are retracted out of the beam line. The NH_3 molecules are ionised by a (2+1) REMPI scheme at 312.4 nm via the $\tilde{B}$ ($v' = 5$) excited state [17] using a focused nanosecond laser with energy up to 10 mJ/pulse.

The ions generated by REMPI are created between a repeller plate and an extractor plate in a Wiley–McLaren time-of-flight (TOF) mass spectrometer (MS). The potential difference between the repeller and extractor accelerates ions into a free flight region; the ions are detected at the end of the flight tube by a

chevron microchannel plate (MCP) stack biased at a high negative voltage (Photonis MCP 25/12/10/12 D 60:1, chevron stack). A commercial amplifier (Stanford Research Systems, Model SR445A) is used to transmit the signal to a digital oscilloscope. For both species of interest in this work, the repeller plate on the TOF-MS is set at 1000 V and the extractor plate at 100 V. For H, the ion signal on the MCPs is detected with a bias voltage of −2000 V. For NH_3, the bias voltage is decreased to −1700 V. The differences in bias voltages are taken into consideration in the data analysis.

TOF profiles are recorded by varying the delay between the pulsed valve (or the excimer photodissociation laser, in the case of H) and the detection laser, to obtain the timing of the peak in the molecular or atomic beam. Once the delay is optimised, it is then kept constant. Beam density measurements are taken by recording the ion signal while varying the laser intensity. The laser energy is measured using an energy meter (Gentec-EO) placed at the viewport where the laser exits the chamber, and recorded using in-built software on a USB flash drive. For each set of measurements, the laser energy is recorded for at least 15 s, and the mean energy and standard deviation calculated. Using the relation $P = E/t$, where E is the laser energy (in J), and t is the laser pulse width (in s), the laser power P (in W) can be calculated. With $I = P/A$, where A (in cm^2) is the laser spot size, the intensity I (in W cm^{-2}) can therefore be calculated.

To measure the intensity of the ion signal, the oscilloscope trace at each energy is recorded as an average of 256 sweeps. After baseline subtraction, the integrated area of the signal is calculated and converted into absolute ion counts using a calibration curve provided by Coulomb crystal Molecular Dynamics (CCMD) simulations [18,19], detailed in the subsection below.

Intense-field laser ionisation studies [8] have demonstrated that, in the limiting case of high laser intensity (where the laser intensity I is greater than the intensity needed to saturate the beam, I_0),

$$\frac{\mathrm{d}S}{\mathrm{d}ln(I/I_0)} = 2\pi\alpha\sigma_r^2 dn_{\mathrm{peak}}, \tag{1}$$

where n_{peak} is the molecular beam peak density, α is the detection efficiency, d is the diameter of the molecular beam, and σ_r is the $e^{-1/2}$ radius of the laser. In this region, a plot of the ion count S against intensity I on a semi-log scale gives the saturation intensity I_0, where the limiting straight line intercepts the x axis. A subsequent plot of S against $\ln(I/I_0)$ gives the slope of the straight line as $2\pi\alpha\sigma_r^2 dn_{\mathrm{peak}}$, allowing the peak number density (n_{peak}) to be obtained. The time-averaged beam density can subsequently be calculated by $n_{\mathrm{average}} = n_{\mathrm{peak}} f_{\mathrm{rep}} \tau_{\mathrm{pulse}}$. In the experiments described here, the laser intensity is varied while the ion count as a function of laser intensity at the peak of the TOF profile at the same detection point is recorded.

In total, the number densities of five molecular and atomic beams are measured, under different sets of conditions. These include: (A) a NH_3 beam; (B) an undecelerated H beam with an average velocity of 560 m s^{-1}; (C) a Zeeman-decelerated H beam (operated at an effective phase angle, ϕ_0, of 40°) with an average decelerated velocity of 350 m s^{-1}; (D) the same Zeeman-decelerated beam as in (C), but with the first pair of Halbach arrays centred on the beam axis, providing a focusing and collimating effect; and (E) a Zeeman-decelerated H beam with an average decelerated velocity of 350 m s^{-1}, obtained using a different coil switching sequence to (C) and (D). The five different sets of measurements will be referred to by their initials henceforth in this article.

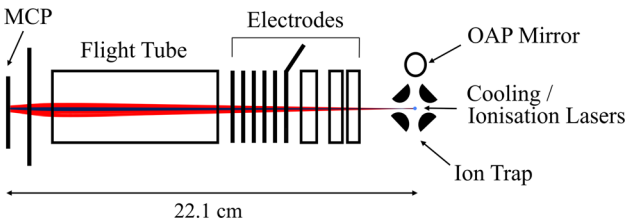

Fig. 2 Schematic diagram (not to scale) showing the key components of the cryogenic ion trap and time-of-flight set-up relevant for this study. Ions are ejected from the trap by switching off the trapping fields and applying 300 V and 165 V to the back and front pairs of trap rods, respectively. Additional voltages can be applied by the electrodes to guide the beam, before the ions enter a field-free flight tube and strike the MCPs. Trajectories are shown for an ejected bicomponent crystal composed of 130 Ca^+ (red) and 40 NH_3^+ (blue) ions. Aside from the trap rods and MCPs, all electrodes are grounded for the simulated trajectories above

2.2 Calibration of the MCPs using CCMD

To calibrate the MCP response and to assign absolute ion numbers, a cryogenic ion trap chamber is used, with a schematic illustration of the key components provided in Fig. 2. Ca atoms are introduced to the ion trap region by a resistively heated Ca oven. Ca atoms are ionised to form Ca^+ ions at the trap centre, using the 355 nm frequency-tripled output of a Nd:YAG laser, before being Doppler cooled with 397 nm and 866 nm diode lasers. The trapped and laser-cooled ions experience competing Coulombic repulsion forces (from neighbouring ions) and confining forces (from the ion trap fields), giving rise to the formation of a Coulomb crystal.

Coulomb crystals of different sizes are formed by varying the experimental parameters. Typical trap parameters involve the application of radiofrequency fields of peak-to-peak amplitude $V_{\mathrm{rf}} = 200$ V and frequency $\Omega_{\mathrm{rf}} = 2.55$ MHz, alongside end-cap voltages of $V_{\mathrm{end}} = 1.25$ V. Images of the fluorescence constantly emitted by the laser-cooled ions are relayed out of the ion trap by a pair of off-axis parabolic mirrors, directed through a microscope lens, and captured by a charge-coupled device (CCD) camera [20,21]. The trapping fields are switched off at a selected time, with static

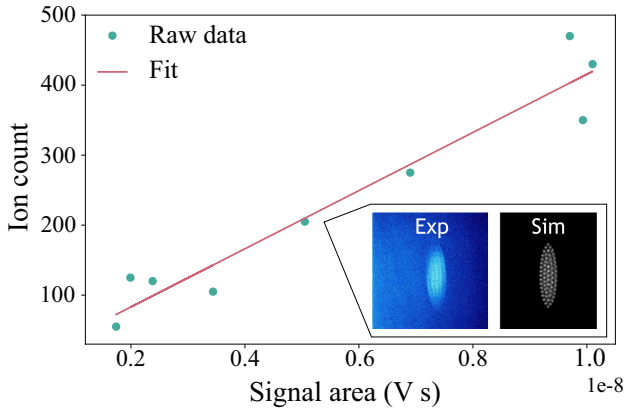

Fig. 3 Calibration curve of the ion count plotted against the integrated signal area obtained from the mass spectra. The inset shows experimental (left) and simulated (right) Coulomb crystal images with 200 ions

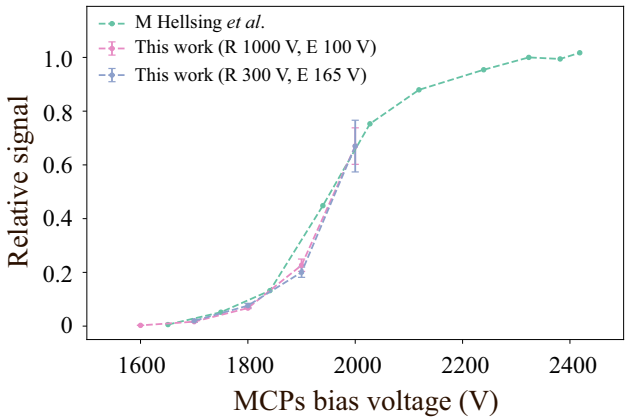

Fig. 4 The relative ion signals recorded as a function of the bias voltage applied to the MCPs (in negative) are plotted. Data taken in this work are compared to findings reported in [23], denoted M Hellsing et al. in the legend, and scaled such that the relative signals at 2000 V are the same. In the legend, R represents the repeller voltage, while E represents the extractor voltage

DC voltages applied to the trapping rods such that two rods act as a repeller pair, and two rods an extractor pair [19,22], ejecting the trapped ions towards the same set of MCPs described above, biased at −2000 V, and connected to the same amplifier used in the number density measurements.

The integrated area of the MCP signal is measured and correlated with the ion numbers obtained from the CCMD simulations of the crystal fluorescence images. The calibration fit is shown in Fig. 3. Due to the physical proximity of the trap rods to one another, repeller and extractor voltages of 1000 V and 100 V (respectively) cannot be used here. Instead, voltages of 300 V and 165 V are applied for the Coulomb crystal measurements—with the different extraction voltages taken into consideration in the data analysis.

2.3 Data analysis procedures

As it is not possible to conduct all of the beam density and calibration experiments under identical experimental conditions, a data scaling procedure is performed to account for the different sets of parameters. To investigate the effect of the MCP voltage on the relative signal size, measurements are taken with all other parameters kept constant. At each MCP bias voltage, five or more repeat scans are recorded, each with 200 sweeps, to obtain the ion signal. Two sets of data are taken at repeller–extractor voltages of 1000 V and 100 V, and one set at 300 V and 165 V. All three data sets show a consistent trend and are in close agreement with previous results [23] when plotted on the same scale (see Fig. 4). It can be seen that the signal obtained at an MCP voltage of −2000 V is approximately 40 times higher than the signal recorded at −1700 V.

To account for the different repeller–extractor voltages used during the number density data acquisition and the CCMD calibration curve data acquisition measurements, a similar approach can be taken. The MCP bias voltage is kept constant at −2000 V, with the repeller–extractor voltages varied. The signal recorded with repeller–extractor voltages of 300 V-165 V is 20% of that recorded at 1000 V-100 V, with all other experimental parameters kept constant. A scaling factor is therefore applied when extracting ion numbers from the Coulomb crystal experiments, to calibrate the signals obtained under the conditions employed for the beam density measurements.

3 Results

To ascertain the beam density for each set of experimental conditions, the variation of ion count against intensity can be plotted on a semi-log scale, as shown in Fig. 5 for a beam of NH_3 molecules. The delay between the pulsed valve and the REMPI detection laser is defined as time t, shown in the inset of the figure. The saturation region is established by considering the number of points that achieve the best linear fit, as defined by the highest coefficient of determination (R^2 value), whilst also ensuring that a sufficient number of points are included for the fit to be meaningful. At least seven points are used for the fit, with a higher number of points used where a higher coefficient of determination could be obtained. The saturation intensity, I_0, can then be obtained from the x-intercept of the graph.

For the dataset presented in Fig. 5, the saturation intensity is 6.3×10^{10} W cm^{-2}. Using this value for saturation intensity, a plot of ion count against ln $\frac{I}{I_0}$ can be obtained, shown in Fig. 6. The slope of this graph equates to $2\pi\alpha\sigma_r^2 dn_{\text{peak}}$, as set out in Eq. 1. The detection efficiency is deemed to be $\alpha = 0.55$, as 55% is the minimum open area ratio of the MCPs given by the manufacturer. The σ_r value is taken to be half the laser beam waist (14.6 μm is the laser beam waist, therefore

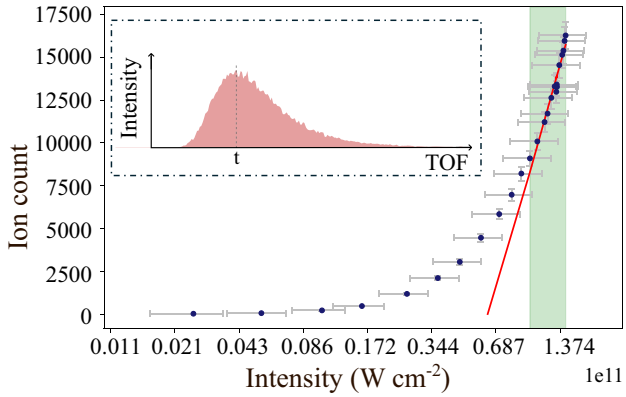

Fig. 5 Ion counts are plotted against intensity for a beam of NH_3 molecules, using a semi-log scale. The inset of the figure shows the delay between the pulsed valve and dye laser, set at time t for the beam density measurements, corresponding to the peak intensity in the TOF profile

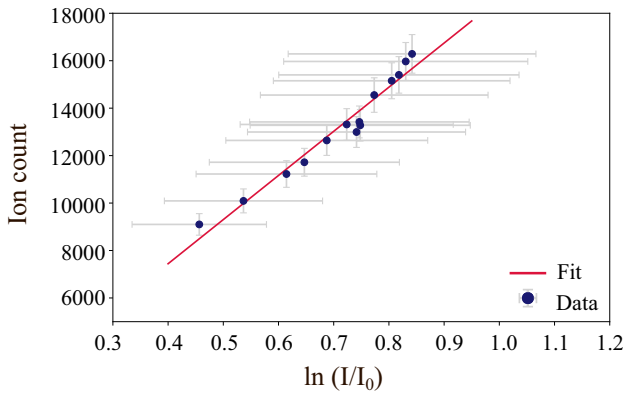

Fig. 6 Ion counts are plotted against $\ln\frac{I}{I_0}$ for the points used to obtain the linear fit in a set of the NH_3 molecular beam density measurements

$\sigma_r = 7.3\ \mu$m). The experimentally measured molecular beam diameter, d, is 10 mm. The resulting gradient of the line of best fit is found to be 1.9×10^4. Using these values, the peak beam density, n_{peak}, for the dataset is calculated at 1.0×10^{10} cm^{-3}, and the time-averaged beam density, $n_{average}$, is 5.6×10^7 cm^{-3}, established using values of 10 Hz for the repetition rate and 550 μs for the pulse duration.

To obtain the absolute density of the beams of H radicals, the same process is repeated. The value of $\alpha = 0.55$ is unchanged, as the MCPs are common to both the NH_3 and H experiments. A value of $\sigma_r = 7.5\ \mu$m is used for H, arising from a minor difference in the laser beam profiles used for the NH_3 and H detection schemes. Measurements are taken for four different H atom beams [(B) to (E)], under the experimental conditions described in Sect. 2.1. Due to the divergence of the beam and the different focusing effects of the decelerator and magnetic fields of the Halbach array on the radicals [16], the diameter of the H radical beam is first determined by translating the laser in the transverse plane, before measurements are taken at the centre of the beam profile. The beam density measurements are repeated twice for each set of experimental conditions, with the results summarised in tabular form in Table 1.

Table 1 Number densities established for the five different (molecular and atomic) beams studied in this work

	n_{peak} (cm^{-3})	$n_{average}$ (cm^{-3})
NH_3 Beam (A)	9.3 (5.2) $\times 10^9$	5.1 (2.9) $\times 10^7$
H Beam (B)	1.2 (0.8) $\times 10^8$	2.9 (1.9) $\times 10^5$
H Beam (C)	8.2 (5.4) $\times 10^7$	2.5 (1.8) $\times 10^4$
H Beam (D)	8.9 (6.3) $\times 10^7$	3.6 (2.7) $\times 10^4$
H Beam (E)	3.2 (2.1) $\times 10^7$	2.3 (1.5) $\times 10^4$

The NH_3 molecular beam (A) has a beam density approximately two orders of magnitude higher than any of the H beams (B–E). Even when considering the different relative gas concentrations in the pre-mix (5% NH_3 in Kr for the NH_3 measurements, versus 10% NH_3 in Kr for the H measurements), there is a disparity in the beam densities. There are almost two orders of magnitude fewer H atoms in beam (A), the undecelerated H atom beam, than in the NH_3 molecular beam—demonstrating the inefficiency of laser photolysis in generating H atoms under the conditions described above. The relative ratios of the beam densities, taking into account the different pre-mix gas mixtures, translates to a photolysis efficiency of approximately 0.5% for the production of H from NH_3.

Unsurprisingly, when comparing the atomic H beams the undecelerated H beam, (B), exhibits the highest density, as the whole beam contributes to the detected signal. Only a subset of H atoms—those in low-field-seeking quantum states and exhibiting an initial velocity and position that enables them to be manipulated by the deceleration sequence—can be successfully decelerated. As such, by considering only the target species (i.e. excluding any non-decelerated H atoms) in the analysis of beams (C) to (E), the intensity of the decelerated H atom beams is necessarily lower than that of the undecelerated beam, (B).

Comparing the densities of the Zeeman-decelerated beam ($\phi_0 = 40°$) with and without the first pair of Halbach arrays in [(D) and (C), respectively], it can be seen that the density is higher when the pair of Halbach arrays are present in the beamline. This can be explained intuitively; when the H atoms come out of the Zeeman decelerator, the beam starts to slightly diverge from the central beam axis. When the first pair of Halbach arrays are present, they act as a focusing element; the magnetic fields exert forces on the target species, causing the beam to become more collimated and increasing the number of H atoms that successfully reach the detection region. The decelerated TOF peak is also broader (i.e. extends over a longer time) when the Halbach arrays are present, causing the time-averaged density to be higher, even though the peak densities are fairly similar. The widths of the peaks can be seen in

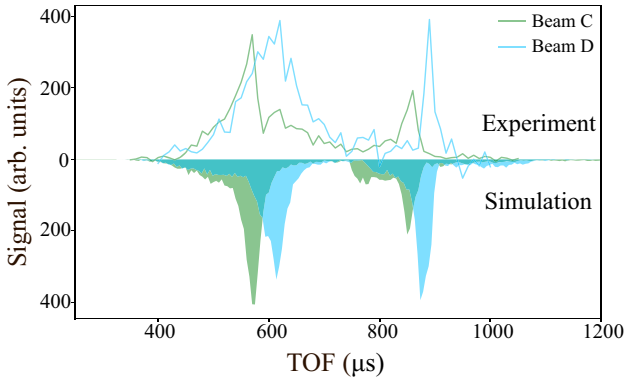

Fig. 7 Experimental (above) and simulated (below, inverted) TOF profiles of a Zeeman-decelerated beam using a standard sequence ($\phi_0 = 40°$), with (Beam D; blue) and without (Beam C; green) the first pair of Halbach arrays positioned on the central beam axis. The faster peak corresponds to the undecelerated H atoms, while the slower peak arises from the decelerated H atoms

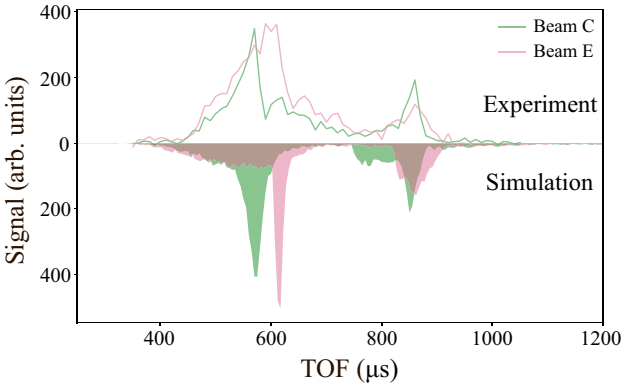

Fig. 8 Experimental and simulated TOF profiles of a Zeeman-decelerated beam using a standard sequence ($\phi_0 = 40°$) (Beam C; green) and a non-standard sequence (Beam E; pink)

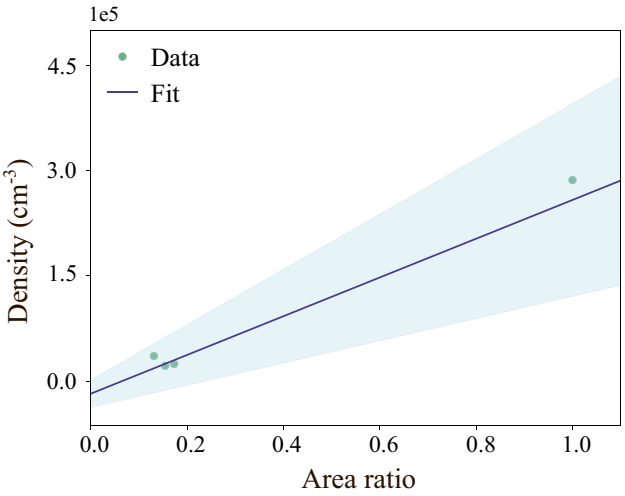

Fig. 9 A plot of the relationship between the area ratio and the time-averaged number density for H atom beams. The error of the linear fit is shown by the shaded blue region

the simulated and experimental TOF traces, shown in Fig. 7.

The simulated TOF profiles are generated by three-dimensional particle trajectory simulations, where H radicals with a distribution of initial positions and velocities are propagated through the fields of the decelerator, the Halbach arrays (if present), and finally reach the detection region [15]. The peak in the TOF traces (see Figs. 7 and 8) with the earlier arrival time corresponds to the bunch of particles that are undecelerated, while the peak with the later arrival time corresponds to the slower particles—our target species.

It is also possible to directly compare beam (C) with beam (E), as the final velocity of the target H atoms in both cases is $350\,\mathrm{m\,s^{-1}}$. As noted above, beam (C) uses a standard Zeeman deceleration sequence ($\phi_0 = 40°$) whilst beam (E) uses a different, non-sequentially lengthening switching sequence for deceleration, chosen arbitrarily. As shown in Fig. 8 and Table 1, a higher peak and time-averaged beam density is seen in the decelerated H atoms produced by beam (C) compared to beam (E).

Based on the experimental measurement of four different H beams, a relationship can be drawn between the time-of-flight data and the number density data. For each H beam involving Zeeman deceleration, (C) to (E), the target species of interest lie solely in the decelerated peak. The area of the decelerated peak (e.g. the area under the curve after ~760 μs in the experimental TOF spectrum recorded for Beam C, as shown in Fig. 7) can be compared to the total integrated area under the TOF curve. The ratio of the area of the decelerated peak to the area under the whole TOF trace provides an indication of the efficiency of Zeeman deceleration, for a given set of experimental parameters. A linear relationship can be obtained between this area ratio and the time-averaged number density of the beam, as shown in Fig. 9. The time-averaged density was chosen for this purpose, as opposed to the peak density, as it more accurately reflects the whole decelerated peak instead of a single point at a single time delay in the peak, which can be subject to higher uncertainties (especially for sharp features). While more data points would be beneficial to reduce the uncertainty in the fit, the data we have available provide a starting point for extracting beam densities from time-of-flight profiles and verifying previous experimental measurements taken with the same apparatus.

In particular, the measurements reported in this work make it possible to benchmark the simulations and provide a reference database of beam density measurements recorded under different conditions, allowing future measurements to be compared against one another more straightforwardly. Using the relationship between the area ratio and number density provided in Fig. 9, it will be possible to estimate H atom beam densities directly from the experimental time-of-flight data.

4 Discussion

Accurately and precisely measuring the density of atomic and molecular beams has been long-acknowledged as a challenging undertaking, and one prone to error. While most pulsed supersonic expansion methods operate in a similar way, the densities of the beams produced are influenced by a plethora of variable factors. These variables include: the valve design and nozzle diameter; the gas pulse width; the properties of the target species; the presence (and identity) of any carrier gases; the backing pressure behind the valve; the temperature of the valve; the vacuum achieved in the chamber the gas is expanded into; the presence of additional elements in the beamline (such as skimmers and focusing or filtering components); the distance from the valve where the density is probed; and many other parameters. In addition to the vast range of valve operating conditions, some species—such as the H atoms studied in this work—are not present in the initial gas mixture, and are produced from precursor species by methods such as photodissociation, discharge, or pyrolysis [24].

The convolution of the multitude of factors that influence the production of supersonic beams has resulted in a wide range of beam densities being reported under different experimental conditions. There are also a variety of methods that can be used to determine experimental beam densities, ranging from calculations based on pressure rises [2,3], to electron-based ionisation processes (such as the use of fast ionisation gauges) [2–4], to quadrupole mass spectrometer detection [7], and to laser-based detection schemes [6,10,11,25–27]. It can be difficult to exclude contributions from background (or seed) gases when beam densities are based solely on measurements that are not species- or mass-selective, resulting in potential overestimation of the true values [3]. While laser-based techniques are highly specific to the species of interest, they require the presence of appropriate detection schemes and sufficiently high laser powers to achieve signal saturation. Nonetheless, it is possible to compare (at least qualitatively) the findings reported in this work to previously reported beam density measurements, to highlight the significant impact of the experimental conditions.

Molecular beams are often quoted as achieving densities on the order of 10^{13}–10^{14} cm^{-3} [1,2,25,28]. Newer piezo-valve designs have achieved reported densities of $\sim 10^{15}$ cm^{-3} (for the Nijmegen pulsed valve) [3], and 10^{14}–10^{18} cm^{-3} (for the Even–Lavie valve) [4]. These values were typically established using a combination of one or more generally applicable methods, such as simulations, fast ionisation gauge responses, and beam brightness measurements [2–4]. The NH_3 beam density reported here is significantly lower than these literature values. Key factors that are likely to reduce the NH_3 molecular beam density by several orders of magnitude include the use of a General valve, modest backing pressure, the significant distance between the valve and where the beam density is probed (with a skimmer and 12 Zeeman decelerator coils present in the beamline), and the use of a seeded molecular beam (where NH_3 makes up only 5% of the gas mixture). In this work, the molecular beam density is recorded under typical operating conditions; some previous findings may be reporting the maximum achievable values using a given valve. (Unless stated otherwise, literature values are assumed to represent average number densities, as opposed to peak densities.)

Laser-based beam density measurements have reported comparatively lower values, more consistent with our findings—although, as each study involved a unique set of experimental conditions, the absolute densities cannot be directly quantitatively compared. A density of 10^7 cm^{-3} was measured for OCS molecules seeded in helium, produced by an Even–Lavie valve [10]. Similarly, the peak and average densities of dibromobutadiene seeded in neon were reported to be 10^7 cm^{-3} and 10^6 cm^{-3}, respectively, using an Amsterdam pulsed valve [11]. The peak density of 9.3×10^9 cm^{-3} and average density of 5.1×10^7 cm^{-3} reported here for NH_3 seeded in krypton are consistent with the literature values for molecular beam densities recorded using laser-based methods.

Beam density studies have also been performed on species that were manipulated by external fields. For example, estimated densities on the order of 10^6–10^8 molecules cm^{-3} were reported for Stark-decelerated metastable CO beams, seeded in xenon and produced by a Jordan valve [26,29]. In another study, the peak density of a Stark-decelerated packet of ND_3 molecules produced by a Nijmegen pulsed valve was estimated to be 10^{10} cm^{-3} [25] (with the average beam density anticipated to be a few orders of magnitude lower).

Prior measurements have also been taken on radical beams, with the species of interest produced from precursor molecules in the initial gas mixture. Discharge methods have seen radical beam densities on the order of 10^{11} cm^{-3} (achieved with a Nijmegen pulsed valve and a dielectric barrier discharge source, and Jordan valve with a DC discharge) [6,27] and 10^{10} cm^{-3} (from a General valve with a DC discharge) [5]. For radicals produced by photodissociation, the beam density measurements are significantly lower—consistent with the lower efficiency of production. SD radicals formed by photodissociation of D_2S following expansion through a General valve have achieved beam densities of $(1.1 \pm 0.1) \times 10^5$ cm^{-3}, measured by monitoring the SD laser-induced fluorescence signal [30]. These experimental conditions represent the closest match to the conditions adopted in this work, and the beam density is in excellent agreement with the (non-decelerated) H atom radical beam density measured here, $(2.9 \pm 1.9) \times 10^5$ cm^{-3}.

5 Conclusions

The absolute number densities of pulsed supersonic beams of ammonia molecules and hydrogen atoms are reported, providing the first experimental mea-

surements for these species using laser-based detection methods, and providing number densities for a novel range of experimental conditions. An average beam density of 5.1×10^7 cm^{-3} is reported for the ammonia beam, with average densities ranging from 2.3–3.6 $\times 10^4$ cm^{-3} [for the subset of successfully decelerated H atoms within the distribution, beams (C) to (E)] to 2.9×10^5 cm^{-3} [for beam (B), the undecelerated H atom beam] for the different atomic hydrogen beams. The presence of a pair of Halbach arrays centred on the beam axis can focus and collimate the target species, increasing the average radical beam density from 2.5×10^4 cm^{-3} to 3.6×10^4 cm^{-3}, with all other parameters unchanged. While the molecular and atomic beam densities reported in this work are significantly lower than some literature values, they are consistent with beam densities recorded under comparable experimental conditions and employing laser-based detection methods. The significant variation in the densities reported for pulsed supersonic beams—spanning some 14 orders of magnitude, when considering all previously reported values—emphasises the importance of taking careful and precise measurements for each species and set of experimental conditions.

The series of measurements presented in this work have also enabled three-dimensional particle trajectory simulations and time-of-flight data to be benchmarked to absolute number densities. While previous studies achieved relative comparisons—for example, demonstrating that the relative number of Zeeman-decelerated H atoms reaching the detection region is higher with the magnetic guide in place than without—it was not previously possible to assign a number density to these beams. Armed with the analysis reported here, and the trend obtained from Fig. 9, it is now possible to estimate the number density of target H atoms directly from TOF traces for measurements performed using the same experimental apparatus. Beam density measurements are critical for bimolecular rate coefficient calculations and, as the significant variation in values highlights, it is imperative that reliable number densities be included in such calculations in order for accurate reaction rate information to be obtained.

Author contributions

BRH conceived the study; RP and LYW were responsible for methodology; LYW was involved in writing—original draft preparation; BRH acquired the funding; and BRH and RP participated in supervision. All authors took part in formal analysis and investigation, and writing—reviewing and editing.

Funding: B.R.H. is grateful to the European Commission (ERC Starting Grant Project 948373) and the Leverhulme Trust (RPG-2022-264) for funding.

Data Availability Statement This manuscript has associated data in a data repository. [Authors' comment: DataCat, the University of Liverpool Research Data Catalogue) and can be accessed at: https://doi.org/10.17638/datacat.liverpool.ac.uk/2794.]

Declarations

Conflict of interest The authors have no relevant financial or non-financial interests to disclose.

References

1. G. Scoles, D. Bassi, U. Buck, D. Laine (eds.), *Atomic and Molecular Beam Methods*, vol. 1 (Oxford University Press, New York, 1988), p.721
2. D. Irimia, R. Kortekaas, M.H.M. Janssen, In situ characterization of a cold and short pulsed molecular beam by femtosecond ion imaging. Phys. Chem. Chem. Phys. **11**(20), 3958 (2009). https://doi.org/10.1039/b822960k
3. B. Yan, P.F.H. Claus, B.G.M. Oorschot, L. Gerritsen, A.T.J.B. Eppink, S.Y.T. Meerakker, D.H. Parker, A new high intensity and short-pulse molecular beam valve. Rev. Sci. Instrum. **84**(2), 023102 (2013). https://doi.org/10.1063/1.4790176
4. U. Even, Pulsed supersonic beams from high pressure source: simulation results and experimental measurements. Adv. Chem. **2014**, 1–11 (2014). https://doi.org/10.1155/2014/636042
5. K. Ikejiri, H. Ohoyama, Y. Nagamachi, T. Teramoto, T. Kasai, A highly intense state-selected OH beam source by the pulsed electric dc discharge method. Chem. Phys. Lett. **379**(3–4), 255–260 (2003). https://doi.org/10.1016/j.cplett.2003.08.040
6. L. Ploenes, D. Haas, D. Zhang, S.Y.T. Meerakker, S. Willitsch, Cold and intense OH radical beam sources. Rev. Sci. Instrum. **87**(5), 053305 (2016). https://doi.org/10.1063/1.4948917
7. K. Okada, K. Sakimoto, Y. Takada, H.A. Schuessler, A study of the translational temperature dependence of the reaction rate constant between CH_3CN and Ne^+ at low temperatures. J. Chem. Phys. **153**(12), 124305 (2020). https://doi.org/10.1063/5.0013807
8. S.M. Hankin, D.M. Villeneuve, P.B. Corkum, D.M. Rayner, Intense-field laser ionization rates in atoms and

molecules. Phys. Rev. A **64**, 013405 (2001). https://doi.org/10.1103/PhysRevA.64.013405
9. C. Meng, A.P.P. Poel, C. Cheng, H.L. Bethlem, Femtosecond laser detection of Stark-decelerated and trapped methylfluoride molecules. Phys. Rev. A **92**, 023404 (2015). https://doi.org/10.1103/PhysRevA.92.023404
10. J. Wiese, J.-F. Olivieri, A. Trabattoni, S. Trippel, J. Küpper, Strong-field photoelectron momentum imaging of OCS at finely resolved incident intensities. New J. Phys. **21**(8), 083011 (2019). https://doi.org/10.1088/1367-2630/ab34e8
11. A. Kilaj, J. Wang, P. Straňák, M. Schwilk, U. Rivero, L. Xu, O.A. Lilienfeld, J. Küpper, S. Willitsch, Conformer-specific polar cycloaddition of dibromobutadiene with trapped propene ions. Nat. Commun. **12**(1), 6047 (2021). https://doi.org/10.1038/s41467-021-26309-5
12. K. Dulitz, M. Motsch, N. Vanhaecke, T.P. Softley, Getting a grip on the transverse motion in a Zeeman decelerator. J. Chem. Phys. (2014). https://doi.org/10.1063/1.4866906
13. J. Toscano, C.J. Rennick, T.P. Softley, B.R. Heazlewood, A magnetic guide to purify radical beams. J. Chem. Phys. **149**(17), 174201 (2018). https://doi.org/10.1063/1.5053656
14. O. Mohamed, L.Y. Wu, A. Tsikritea, B.R. Heazlewood, Optimizing the intensity and purity of a Zeeman-decelerated beam. Rev. Sci. Instrum. **92**(9), 093201 (2021). https://doi.org/10.1063/5.0061379
15. J. Toscano, A. Tauschinsky, K. Dulitz, C.J. Rennick, B.R. Heazlewood, T.P. Softley, Zeeman deceleration beyond periodic phase space stability. New J. Phys. **19**(8), 083016 (2017). https://doi.org/10.1088/1367-2630/aa7ef5
16. J. Toscano, M. Hejduk, H.G. McGhee, B.R. Heazlewood, Manipulating hydrogen atoms using permanent magnets: characterisation of a velocity-filtering guide. Rev. Sci. Instrum. **90**(3), 033201 (2019). https://doi.org/10.1063/1.5078573
17. E.W. Steer, L.S. Petralia, C.M. Western, B.R. Heazlewood, T.P. Softley, Measurement of the orientation of buffer-gas-cooled, electrostatically-guided ammonia molecules. J. Mol. Spectrosc. **332**, 94–102 (2017). https://doi.org/10.1016/j.jms.2016.11.003
18. A. Tsikritea, K. Park, P. Bertier, J. Loreau, T.P. Softley, B.R. Heazlewood, Inverse kinetic isotope effects in the charge transfer reactions of ammonia with rare gas ions. Chem. Sci. **12**, 10005–10013 (2021). https://doi.org/10.1039/D1SC01652K
19. K.A.E. Meyer, L.L. Pollum, L.S. Petralia, A. Tauschinsky, C.J. Rennick, T.P. Softley, B.R. Heazlewood, Ejection of Coulomb crystals from a linear Paul ion trap for ion–molecule reaction studies. J. Phys. Chem. A **119**(50), 12449–12456 (2015). https://doi.org/10.1021/acs.jpca.5b07919
20. M. Hejduk, B.R. Heazlewood, Off-axis parabolic mirror relay microscope for experiments with ultra-cold matter. Rev. Sci. Instrum. (2019). https://doi.org/10.1063/1.5123792
21. C. Miossec, M. Hejduk, R. Pandey, N.J.A. Coughlan, B.R. Heazlewood, Design and characterization of a cryogenic linear Paul ion trap for ion–neutral reaction studies. Rev. Sci. Instrum. **93**(3), 033201 (2022). https://doi.org/10.1063/5.0080458
22. N. Deb, L.L. Pollum, A.D. Smith, M. Keller, C.J. Rennick, B.R. Heazlewood, T.P. Softley, Coulomb crystal mass spectrometry in a digital ion trap. Phys. Rev. A (2015). https://doi.org/10.1103/physreva.91.033408
23. M. Hellsing, L. Karlsson, H.-O. Andren, H. Norden, Performance of a microchannel plate ion detector in the energy range 3–25 keV. J. Phys. E: Sci. Instrum. **18**(11), 920 (1985). https://doi.org/10.1088/0022-3735/18/11/009
24. L.Y. Wu, C. Miossec, B.R. Heazlewood, Low-temperature reaction dynamics of paramagnetic species in the gas phase. Chem. Commun. **58**(20), 3240–3254 (2022). https://doi.org/10.1039/d1cc06394d
25. S.N. Vogels, Z. Gao, S.Y. Meerakker, Optimal beam sources for Stark decelerators in collision experiments: a tutorial review. EPJ Tech. Instrum. (2015). https://doi.org/10.1140/epjti/s40485-015-0021-y
26. J.R. Bochinski, E.R. Hudson, H.J. Lewandowski, G. Meijer, J. Ye, Phase space manipulation of cold free radical OH molecules. Phys. Rev. Lett. (2003). https://doi.org/10.1103/physrevlett.91.243001
27. M.C. Beek, J.J. Meulen, An intense pulsed electrical discharge source for OH molecular beams. Chem. Phys. Lett. **337**(4–6), 237–242 (2001). https://doi.org/10.1016/s0009-2614(01)00223-8
28. A. Libson, M. Riedel, G. Bronshtein, E. Narevicius, U. Even, M.G. Raizen, Towards coherent control of supersonic beams: a new approach to atom optics. New J. Phys. **8**(5), 77–77 (2006). https://doi.org/10.1088/1367-2630/8/5/077
29. H.L. Bethlem, G. Berden, G. Meijer, Decelerating neutral dipolar molecules. Phys. Rev. Lett. **83**(8), 1558–1561 (1999). https://doi.org/10.1103/physrevlett.83.1558
30. A. Mizouri, L.Z. Deng, J.S. Eardley, N.H. Nahler, E. Wrede, D. Carty, Absolute density measurement of SD radicals in a supersonic jet at the quantum-noise-limit. Phys. Chem. Chem. Phys. **15**(45), 19575 (2013). https://doi.org/10.1039/c3cp53394h